



# Tuning interaction between cobalt catalysts and nitrogen dopants in carbon nanospheres to promote Fischer-Tropsch synthesis

Qingpeng Cheng<sup>a</sup>, Na Zhao<sup>a</sup>, Shuaishuai Lyu<sup>a</sup>, Ye Tian<sup>a</sup>, Fei Gao<sup>b</sup>, Lin Dong<sup>b</sup>, Zheng Jiang<sup>c</sup>, Jing Zhang<sup>d</sup>, Noritatsu Tsubaki<sup>e</sup>, Xingang Li<sup>a,\*</sup>

<sup>a</sup> Collaborative Innovation Center of Chemical Science and Engineering (Tianjin), Tianjin Key Laboratory of Applied Catalysis Science and Technology, School of Chemical Engineering and Technology, Tianjin University, Tianjin, 300072, PR China

<sup>b</sup> Jiangsu Key Laboratory of Vehicle Emissions Control, Lab of XPS, Center of Modern Analysis, School of Environment, Nanjing University, Nanjing, 210093, PR China

<sup>c</sup> Shanghai Synchrotron Radiation Facility, Shanghai Institute of Applied Physics, Chinese Academy of Sciences, Shanghai, 201800, PR China

<sup>d</sup> Beijing Synchrotron Radiation Facility, Institute of High Energy Physics, Chinese Academy of Sciences, Beijing, 100049, PR China

<sup>e</sup> Department of Applied Chemistry, School of Engineering, University of Toyama, Gofuku 3190, Toyama, 930-8555, Japan

## ARTICLE INFO

### Keywords:

N-doped carbon materials  
Fischer-Tropsch synthesis  
Co catalysts  
Pyrrolic N  
Co-N interaction

## ABSTRACT

N-doped carbon supports are promising to improve reduction degree and dispersion of metal catalysts in Fischer-Tropsch synthesis (FTS). However, it is a great challenge to reasonably construct desired N dopants on FTS catalysts. Herein, we report the high FTS performance of the Co catalysts supported on N-doped carbon nanospheres synthesized by using a facile strategy. Through precisely tailoring the N dopants, we discover that the interaction between cobalt catalysts and supports is significantly strengthened via donation electron function of N atoms, especially for pyrrolic N. It improves the dispersion of cobalt species to generate more electron-enriched cobalt sites, which can strongly adsorb CO and accelerate CO dissociation to C\*, resulting in the enhanced catalytic activity. In addition, these in turn increase C\* concentration on the surface of the active cobalt sites, which is favorable to form a high concentration of chain initiators CH<sub>2</sub> to stimulate carbon-chain growth, inducing the high selectivity towards the C<sub>5</sub><sup>+</sup> products in FTS. Accordingly, the Co/NCS-500 catalyst with the high content of pyrrolic N presents the high FTS activity and C<sub>5</sub><sup>+</sup> selectivity. Our work provides a new avenue in rational development of other related heterogeneous catalysis.

## 1. Introduction

Rapid depletion of petroleum reserves and environmental degradations spark extensive research on alternative feedstocks to produce valuable chemicals and liquid fuels [1]. Fischer-Tropsch synthesis (FTS) can transfer syngas (CO/H<sub>2</sub>), derived from non-petroleum-based carbon sources, into environmentally valuable chemicals, which is a sustainable strategy of great significance [2,3]. Cobalt-based metal catalysts have been widely investigated because of their high selectivity towards long-chain paraffins and long-term active lifetime [3–5]. Carbon materials are promising candidates as supports because of the inherent inertness of their surfaces to generate a weak metal-support interaction, which is readily to achieve a high reduction degree of metal catalysts. However, active metal species may easily aggregate on carbon-based supports during reactions. In general, cobalt-based catalysts are expected to possess both high reduction degree and dispersion to improve the utilization efficiency of metallic cobalt. Thus, how to

balance the contradiction between the two factors is one of the important challenges in FTS.

Generally, surface properties of carbon supports can be tailored according to requirements of reaction systems [6,7]. Heteroatom-doped strategy is regarded as one of increasingly favored chemical modifications [7–9]. Among the alternative dopant elements, the nitrogen (N) involved modification has attracted worldwide attention on strengthening the interaction between metal and supports to improve the former's dispersion because N dopants can act as electronic donor atoms [10]. It is reported that the metal catalysts modified with N dopants in carbon supports can boost catalytic performance in some specific reactions [11,12].

A great interest has been focused on FTS catalysts supported on N-doped carbon materials [13–27]. Recently, Yang et al. reported that the cobalt supported on N-doped carbon could improve the heavy hydrocarbon selectivity [24], while Fu et al. held the opposite perspective [16]. This controversy may be caused by uncontrollable contents and

\* Corresponding author.

E-mail address: [xingang.li@tju.edu.cn](mailto:xingang.li@tju.edu.cn) (X. Li).

<https://doi.org/10.1016/j.apcatb.2019.02.024>

Received 8 December 2018; Received in revised form 1 February 2019; Accepted 10 February 2019

Available online 11 February 2019

0926-3373/ © 2019 Elsevier B.V. All rights reserved.

types of N dopants in catalysts, which are typically composed of pyridinic N, pyrrolic N and graphitic N. At present, few studies have reported the effect of the types of N dopants on FTS performance, probably because systematically tailoring the N dopants in the catalyst is a great challenge. Recently, Xiong et al. [20] reported the effect of the types of N dopants on FTS performance over Fe catalysts. In their work, the pyrrolic N and pyridinic N played a key role in binding the Fe atoms, and the graphitic N atoms played a minor role. The Fe/NCS catalyst with the high FTS activity was ascribed to the high content of pyrrolic/ pyridinic N atoms. Their work is important to discover the function of the types of N dopants on FTS, but unexpectedly brings the doubt about the influence of the different preparation methods alone on the physicochemical properties of catalysts. In addition, it is worth to note that doping N atoms into catalysts is generally realized by thermal annealing of carbon-based materials at high temperatures in a flow of  $\text{NH}_3$ , HCN, melamine, pyridine, or polypyrrole [13–15,19–21,28–31]. In this process, exhausted harmful N containing gases will cause serious environmental pollution. Therefore, it is urgent to explore a sustainable route to controllably synthesize N-doped carbon-based catalysts, and clearly clarify functions of N dopants on FTS, as well.

Carbon nanospheres (CS), randomly composed of curly graphitic flakes with  $sp^2$  hybridization, are frequently considered as model supports because of their inert and nonporous properties [20]. Herein, we synthesized a series of homogeneously dispersed and size-controlled N-doped carbon nanospheres (NCS) via a simple strategy, using biomolecule dopamine as the carbon and nitrogen resources. Through adjusting the carbonization temperatures, we can precisely control the contents of the N dopants over the NCS-based materials. We discover that the N dopants in the carbon network, especially for pyrrolic N, can dramatically tailor the interaction between cobalt and support to achieve an improved FTS activity. Compared with the CS supported cobalt catalyst, the Co/NCS-T catalysts possessed the higher catalytic activity and  $\text{C}_5^+$  selectivity. Especially, the Co/NCS-500 catalyst with the highest content of pyrrolic N in all catalysts exhibited more than 2-fold higher in the catalytic reaction rate and 1.5-fold higher in the  $\text{C}_5^+$  selectivity.

## 2. Experimental

### 2.1. Catalyst preparation

#### 2.1.1. Preparation of the N-doped carbon nanospheres (NCS)

Polydopamine (PDA) nanospheres were synthesized by a previously reported method [32]. Ammonia aqueous solution of 2 mL ( $\text{NH}_4\text{OH}$ , 28–30%) was mixed with ethanol of 40 mL and deionized water of 90 mL under mild stirring at room temperature for 0.5 h. Dopamine hydrochloride with the molar ratio of ammonia to dopamine of 10.6 was dissolved in deionized water of 10 mL and then added dropwise to the above mixed solution. The color of this solution promptly changed to pale brown and then gradually turned to dark brown. The synthesis process of PDA nanospheres was continued for 30 h. The PDA nanospheres were acquired by centrifugation and washing with deionized water for three times. The average size of PDA nanospheres could be easily controlled through tuning the molar ratio of ammonia to dopamine hydrochloride (pH value). The pH values used for synthesis of PDA nanospheres at 340, 200, and 160 nm were 9.44, 9.68, and 9.77, respectively. The NCS-T materials were obtained via carbonizing the PDA nanospheres at 500, 600, 700 and 800 °C for 1 h at a rate of 5 °C min<sup>-1</sup> in  $\text{N}_2$  flow. The “T” stands for the carbonization temperature.

#### 2.1.2. Preparation of the Co/NCS-T

The Co/NCS-T catalysts were prepared by an ultrasonic-assisted wetness impregnation method. The as-synthesized NCS-T supports of 2.0 g were added to ethanol solution of 10 mL containing cobalt acetate of 0.26 g. Then, the mixed solutions were treated under ultrasonic for

2 h, transferred in a beaker, stirred, and condensed to dryness at room temperature. Finally, the black powder was calcined at 400 °C for 4 h at a rate of 2 °C min<sup>-1</sup> in  $\text{N}_2$  flow. The obtained catalysts were labeled as Co/NCS-T, where “T” equaled to the carbonization temperature. The actual loading of the Co/NCS-T catalysts was ~3.0 wt. % calculated from the thermogravimetry (TG) results.

#### 2.1.3. Preparation of the Co/CS

The glucose polymer (GP) nanospheres were prepared by a hydrothermal method using glucose as a carbon source [33]. Briefly, glucose of 4 g was dissolved in deionized water of 40 mL to form a clarified liquid, and then the mixed solution was poured into a teflon-sealed autoclave of 50 mL and maintained at 160 °C for 3 h. The carbon nanospheres (CS) were obtained by carbonizing GP nanospheres at 500 °C in  $\text{N}_2$  flow. The preparation process of the Co supported CS catalyst was the same with the Co/NCS-T catalysts. The actual loading of the Co/CS catalyst was ~3.0 wt. % calculated from the TG results.

### 2.2. Catalyst characterization

Thermogravimetric analysis (TGA) was carried out on a DTG-60 (Shimadzu) using air or  $\text{N}_2$  as the purge gas to investigate the cobalt content or the thermal stability, respectively. The sample was heated to 800 °C at a rate of 10 °C min<sup>-1</sup> in purge gas of 30 mL min<sup>-1</sup>.

Inductively coupled plasma optical emission spectrometry (ICP-OES) was carried out on a Thermo Scientific iCAP 6500 to the mass fraction of cobalt in all the catalysts.

Scanning electron microscopy (SEM) images and energy dispersive spectroscopy (EDS) mappings were taken on a Hitachi S-4800 microscope at 3 kV. Transmission electron microscopy (TEM) images were taken on a JEM-2100 F microscope at 200 kV. The particle size distributions were obtained upon the measurement of 200 particles from several TEM images taken at diverse positions of TEM grid. The surface-averaged particle size was calculated from  $d(\text{Co}^0) = \frac{\sum n_i d_i^3}{\sum n_i d_i^2}$  with the

standard deviation of  $\sigma = \sqrt{\frac{\sum n_i \cdot (d_i - d(\text{Co}^0))^2}{\sum n_i}}$ , where  $n_i$  was the frequency of occurrence of each  $d_i$  size. The dispersion ( $D$ ) of the catalyst could be calculated from the surface-averaged  $\text{Co}^0$  particle size by assuming a spherical geometry of the metal particles with uniform site density of 14.6 atoms nm<sup>-2</sup> as described in using  $D = \frac{96}{d(\text{Co}^0)}$  [34,35].

Fourier transform infrared (FTIR) spectra were recorded on a Nicolet Nexus IR spectrometer in the range of 1000–4000 cm<sup>-1</sup> with a resolution of 2 cm<sup>-1</sup> and accumulation of 32 scans.

Ex situ XPS measurements were performed in a ThermoFisher Scientific ESCALAB 250XI with the monochromatic Al K $\alpha$  line (1486 eV). The described data in this work were obtained from ex situ XPS without special instruction.

In situ XPS spectra were measured on a PHI 5000 Versa Probe with an aluminum monochromatic Al K $\alpha$  line (1486 eV). Before providing the samples for the in situ XPS experiments, we pre-reduced the sample for 10 h at 400 °C in a high purity hydrogen flow, and then protected them with  $\text{N}_2$  to prevent their contact with air. The as-prepared sample mixed with inert silica of the same weight was pressed into a disk with a diameter of 10 mm and placed in the introduction chamber (IC), and then was transferred to the reaction chamber (RC) by a transfer rod. The sample was reduced in 7 vol. %  $\text{H}_2/\text{Ar}$  flow for 2 h at 400 °C after degassing in RC. The sample was transferred back to IC when the temperature was cooled to room temperature. Subsequently, the sample was transferred to the main chamber for XPS detection with an accuracy at  $\pm 0.1$  eV.

The content of hydrogen, carbon and nitrogen in the samples was determined by CHN elemental analysis (EA) using a Carlo Erba NA1500 analyzer. The content of oxygen was determined by differential subtraction.

The X-ray diffraction (XRD) patterns of the samples were obtained

via a Bruker D8 Advance diffractometer using Cu K $\alpha$  radiation ( $\lambda = 1.5405 \text{ \AA}$ ), scanning  $2\theta$  from  $15$  to  $85^\circ$  using a scanning speed of  $4^\circ \text{ min}^{-1}$  at  $40 \text{ kV}$  and  $40 \text{ mA}$ .

Nitrogen physisorption was measured with a Quantachrome Quadrasorb SI instrument at  $-197^\circ \text{C}$  to obtain the specific surface area. Before the measurement, all the samples were degassed at  $200^\circ \text{C}$  for  $6 \text{ h}$ . The specific surface areas were obtained in a relative pressure range from  $0.05$  to  $0.30$  and were calculated using the Brunauer-Emmett-Teller (BET) method.

Raman spectra were recorded with a Raman spectrometer (inVia reflex, Renishaw) equipped with the cooled charge coupled device (CCD) detector.

The X-ray absorption experiment was conducted by using the transmission mode through a Si (111) double crystal monochromator at 14W1 beamline of the Shanghai Synchrotron Radiation Facility (SSRF) and 1W1B beamline of the Beijing Synchrotron Radiation Facility (BSRF). Calibration and data alignment were performed by using the Athena software. The reference samples were Co-foil, CoO and Co $_3$ O $_4$ .

H $_2$ -temperature programmed reduction (H $_2$ -TPR) measurements were performed by heating the catalysts ( $30 \text{ mg}$ ) up to  $900^\circ \text{C}$  at a rate of  $10^\circ \text{C min}^{-1}$  in  $8 \text{ vol. \% H}_2/\text{N}_2$  flow of  $30 \text{ mL min}^{-1}$  on a TPDRO Chemisorption Analyzer (TP-5080, Xianquan Co.).

CO-temperature programmed desorption/Mass spectrometry (CO-TPD/MS) measurements were performed over the pre-reduced sample at  $400^\circ \text{C}$  for  $10 \text{ h}$  in  $\text{H}_2$  flow. And then, the sample adsorbed CO at  $220^\circ \text{C}$  after purging in He flow at  $400^\circ \text{C}$  for  $1 \text{ h}$ . Then the flow of CO was switched to He and the temperature was maintained at  $220^\circ \text{C}$  for  $1 \text{ h}$ . Finally, the sample was heated from  $220$  to  $850^\circ \text{C}$  at a heating rate of  $10^\circ \text{C min}^{-1}$ , and the signal of CO ( $m/z = 28$ ) was monitored on a mass spectrometer (HPR-20 QIC, Hiden Analytical Ltd.).

### 2.3. Catalyst testing

FTS reactions were performed in an I.D. 6-mm fixed-bed tubular reactor with the fresh catalyst ( $0.2 \text{ g}$ ) mixed with SiC ( $0.2 \text{ g}$ ), which was inert for reaction and acted as a good thermal conductor to control the process temperature. The catalyst was reduced in a pure hydrogen atmosphere at  $400^\circ \text{C}$  for  $10 \text{ h}$  and then cooled to  $100^\circ \text{C}$  before switching to premixed syngas ( $\text{H}_2/\text{CO} = 2$ ). The reaction pressure was regulated by a back-pressure regulator and gradually rose to  $2 \text{ MPa}$ . The catalyst activity testing is maintained at low CO conversion ( $< 10\%$ ). Data were taken at steady state after  $24 \text{ h}$  on stream. The gas effluents were analyzed online by using a gas chromatograph (GC) equipped with a thermal conductivity detector (TCD) and a flame ionization detector (FID). Liquid products and wax were collected in a cold trap and a hot trap, respectively, and then were off-line analyzed on a GC, which was equipped with a HP-1 capillary column.

## 3. Results and discussion

### 3.1. Physicochemical properties of NCS

Fig. 1a schematically illustrates the synthetic strategy for the PDA nanospheres. The biomolecule dopamine containing carbon and nitrogen atoms can self-polymerize and spontaneously deposit PDA films on any surface [32,36,37]. Dopamine directly polymerizes into homogeneously dispersed nanospheres without using any template in a mixture containing water, ethanol, and ammonia at room temperature. The TEM (Fig. 1b) and SEM (Fig. 1c–e) images show that the PDA nanospheres are uniformly spherical and homogeneously dispersed. The average size of the PDA nanospheres can be easily controlled through tuning the molar ratio of ammonia to dopamine hydrochloride from  $5.3$  to  $10.6$  (Fig. 1c–e). Compared with the large-size PDA nanospheres, the smaller ones are favorable for dispersing metal species due to their larger specific surface areas. Thus, we selected the PDA nanospheres with the average size of  $160 \text{ nm}$  for further study in this work. Figure S1

shows the characteristic IR bands of several functional groups of the PDA nanospheres, such as N–H, –OH, C–O, and C–N. The PDA nanospheres are endowed with an active surface for chelating metal cations ascribed to the presence of these functional groups. Both the PDA nanospheres and referential GP nanospheres, synthesized via a hydrothermal method using glucose as a carbon source, have the excellent thermostability in  $\text{N}_2$  atmosphere (Figure S2), which guarantees their successful transition to carbon materials by carbonization [32]. The SEM images in Figure S3 and S4 show that the PDA and GP exist as the homogeneously dispersed nanospheres. The extra N atoms are homogeneously deposited on the PDA nanospheres in Figure S3. Moreover, in Figure S5 the binding energy (BE) peaks located at  $284.6$ ,  $399.8$ , and  $532.9 \text{ eV}$  correspond to C  $1s$  of  $sp^2$  C, N  $1s$  of doped N, and O  $1s$  of oxygen functional groups in the XPS full scan spectra, respectively, which confirms the successful N doping into the PDA nanospheres. Here, the atomic percentage of N in the PDA nanospheres is about  $7.3\%$ , which is in line with the SEM-EDS results in Table S1.

Carbonization of PDA nanospheres (BET surface area =  $30.4 \text{ m}^2 \text{ g}^{-1}$ ) in  $\text{N}_2$  flow can directly convert them to N-doped carbon nanospheres (NCS) without additional treatments. The whole process from the synthesis of the original carbon precursor (PDA nanospheres) to the formation of the NCS is sustainable. Table S2 summarizes the  $\text{N}_2$  physisorption results of the NCS-T supports carbonized at the different temperatures. The surface area of the NCS-T supports slightly decreases from  $345.6$  to  $291.2 \text{ m}^2 \text{ g}^{-1}$  with the elevated carbonization temperatures from  $500$  to  $800^\circ \text{C}$ . It indicates that the carbonization temperature between  $500$  to  $800^\circ \text{C}$  does not significantly affect the texture properties of the NCS-T supports.

Fig. 2 shows the SEM images of the NCS-T supports carbonized at the different temperatures. As expected, the homogeneously dispersed NCS-T supports still maintain an intact structure ascribed to the excellent thermostability of the PDA nanospheres (Figure S2 and S6). The XPS full scan spectra of the NCS-T in Figure S7 confirm the existence of heteroatom N survived from the original PDA nanospheres. Compared with the PDA nanospheres, the oxygen content of the NCS-T supports significantly drops (Table S1 and S2), indicating the successful carbonization [32]. The N content can be easily controlled by tuning the carbonization temperatures (Table S2). Figure S8 shows the function of the N contents determined from the XPS and elemental analysis (EA) results on the carbonization temperatures. The N contents in the NCS-T supports obtained from the XPS decreases from  $9.5$  to  $6.7 \text{ wt. \%}$  with the elevated carbonization temperatures from  $500$  to  $800^\circ \text{C}$ , which is similar to the EA results which decrease from  $10.9$  to  $7.3$ . It is worth noting that XPS is a surface technology that obtains the N content on the surface of the supports; whereas EA analysis is a bulk technique that achieves the total N content in the supports. Thus, there may exist difference between them. In addition, the XRD patterns of the NCS-T in Figure S9 show that the graphitization degree of the NCS-T increases with the elevated carbonization temperatures, as indicated by the strengthened carbon diffraction peak at  $43.8^\circ$  [15,16]. To further determine the graphitization degree of NCS-T, the Raman spectra of the NCS-T supports were obtained in Figure S10. The D band located at  $\sim 1354 \text{ cm}^{-1}$  is assigned to the disordered (defective) carbon, and the G band located at  $\sim 1580 \text{ cm}^{-1}$  is ascribed to the graphite carbon [38,39]. The increased intensity ratio ( $I_D/I_G$ ) of the two peaks indicates a decrease in the graphitization degree [38,39]. In this work, when the carbonization temperatures are elevated from  $500$  to  $800^\circ \text{C}$ , the G band becomes stronger in Figure S10. And the  $I_D/I_G$  values decrease from  $1.03$  for NCS-500 to  $0.80$  for NCS-800 in Table S3, which further indicates that the graphitization degree of the NCS-T increases with the elevated carbonization temperatures.

### 3.2. Physicochemical properties of Co/NCS-T

We prepared a series of the Co/NCS-T catalysts and the reference Co/CS catalyst by an ultrasonic-assisted incipient impregnation

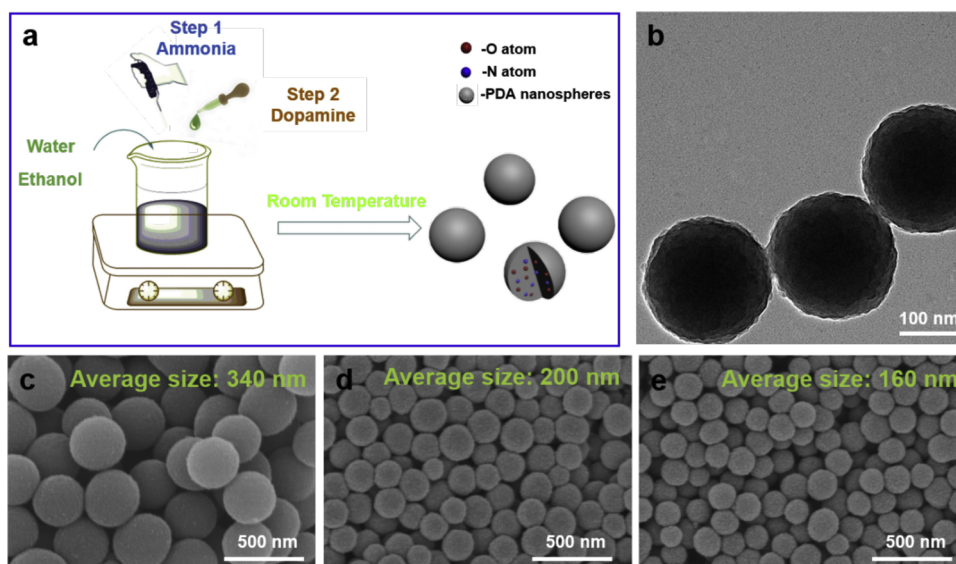


**Fig. 1.** (a) Schematic illustration on the stepwise formation of the PDA nanospheres, (b) TEM image of the PDA nanospheres, (c–e) SEM images of the PDA nanospheres. Molar ratio of ammonia to dopamine hydrochloride: (c) 5.3, (b, d) 8.0 and (e) 10.6.

method. Figure S11 shows the SEM images of the Co/NCS-T catalysts. As expected, after loading cobalt, the resultant catalysts still preserve the homogeneous dispersion, structural integrity, and spherical morphology of the NCS-T supports. The SEM image of the Co/CS catalyst also has a similar trend (Figure S12). Figure S13 shows the XRD patterns of the catalysts. Surprisingly, the existence states of the cobalt species depend on the support. Two kinds of cobalt phases including metallic cobalt and CoO exist on the Co/NCS-500 and Co/NCS-600 catalysts. Nevertheless, we observe the  $\text{Co}_3\text{O}_4$  phase besides the above mentioned two cobalt phases on the Co/NCS-700 and Co/NCS-800 catalysts. The existence of Co and CoO is attributed to the self-reduction of the cobalt precursor on the carbon support. On the Co/CS catalyst, only the diffraction peaks belonging to the CoO phase are observed.

In order to further determine the cobalt species and its content in

the Co/NCS-T catalysts, we conducted the X-ray absorption fine structure (XAFS) experiments. We obtained the contents of the cobalt species in the catalysts by linear fitting of the X-ray absorption near edge structure (XANES) spectra (Fig. 3 and Figure S14) and summarized the corresponding results in Table S4. With the elevated carbonization temperatures from 500 to 800 °C, the molar content of  $\text{Co}_3\text{O}_4$  increases from 0 to 9.3% in Fig. 3. And, the N-free Co/CS catalyst possesses the  $\text{Co}_3\text{O}_4$  content of 11.8% in Figure S14 and Table S4. In addition, the  $\text{Co}_3\text{O}_4$  phase is not observed in the XRD patterns of the Co/CS and Co/NCS-600 catalysts in Figure S13, but the result of the XAFS linear fitting is reversed. The difference may be ascribed to the fact that the  $\text{Co}_3\text{O}_4$  detected by XAFS is in a short-range order (below 3 nm) [40,41], while the  $\text{Co}_3\text{O}_4$  crystallites detected by XRD are in a long-range order (above 5 nm) [42].

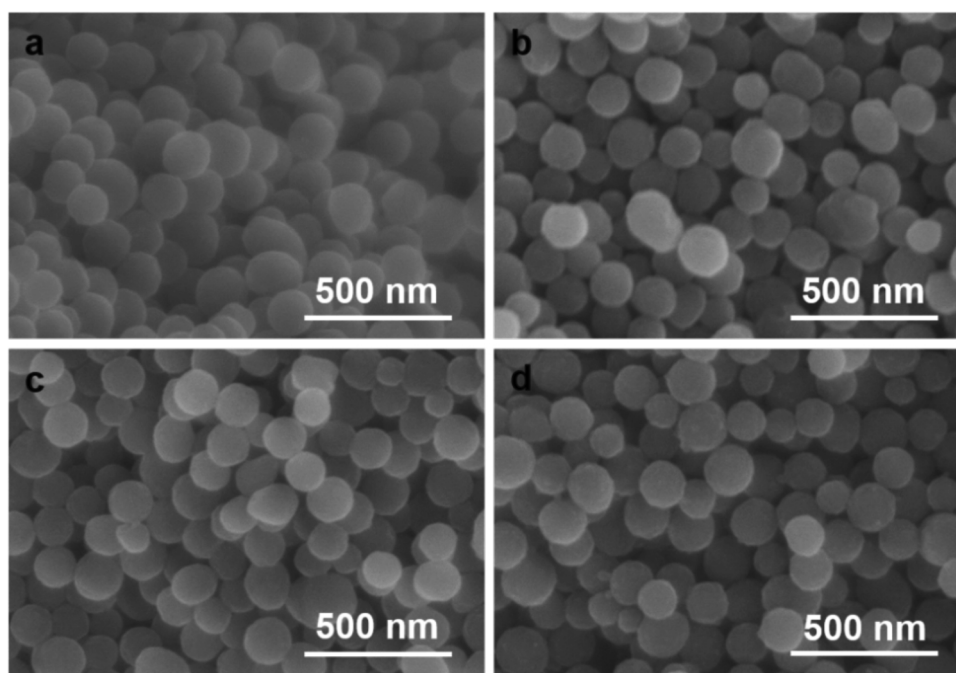


**Fig. 2.** SEM images of the supports (a) NCS-500, (b) NCS-600, (c) NCS-700, and (d) NCS-800. The NCS-T supports are obtained by carbonization of PDA nanospheres with molar ratio of ammonia to dopamine hydrochloride of 10.6.



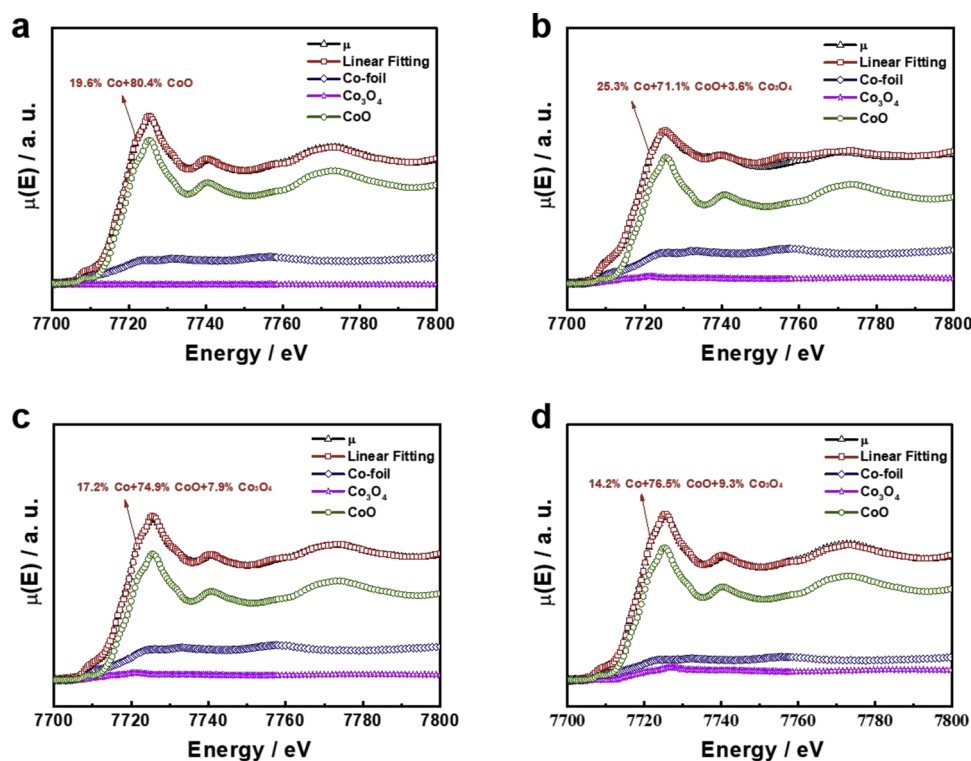


Fig. 3. XANES spectra with fitting curves of the catalysts (a) Co/NCS-500, (b) Co/NCS-600, (c) Co/NCS-700, and (d) Co/NCS-800.

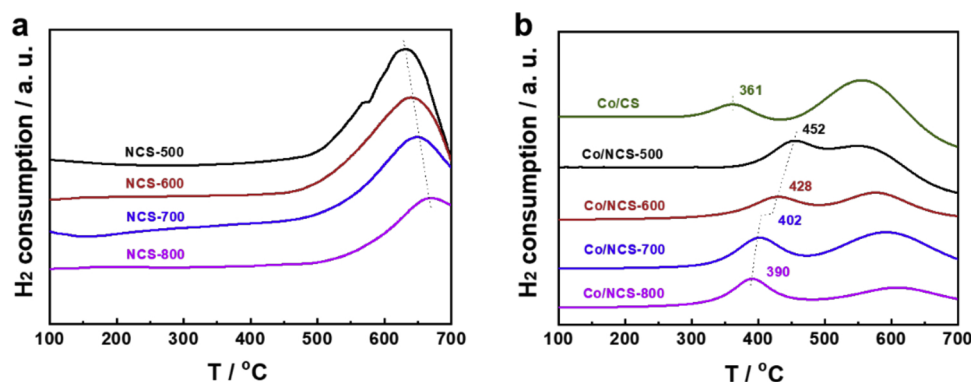
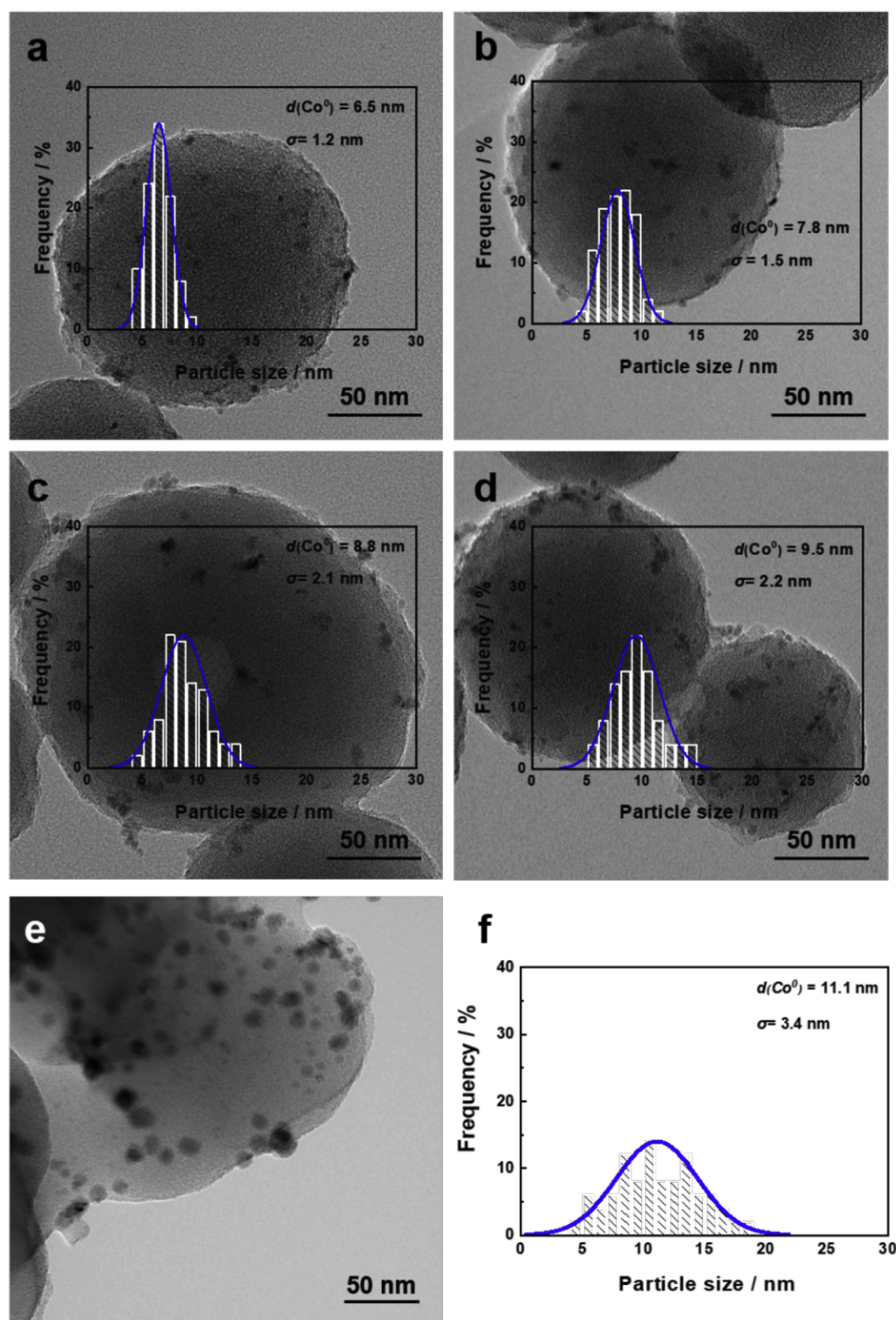


Fig. 4. H<sub>2</sub>-TPR profiles of the (a) NCS-T supports and (b) Co/NCS-T and Co/CS catalysts.

We carried out the H<sub>2</sub>-TPR experiments to investigate the effect of the carbonization temperature on the reduction behavior of the catalysts. Fig. 4 shows the H<sub>2</sub>-TPR profiles of the samples. In Fig. 4a, only one peak located at ~650 °C is observed, which is ascribed to the gasification of the NCS-T supports [43,44]. The gasification temperature increases with the elevated carbonization temperatures of the supports. It indicates that the NCS-800 possesses the highest graphitization degree among the NCS-T supports, which is consistent with the XRD (Figure S9) and Raman (Figure S10) results. Two reduction peaks are observed on the profiles of the Co/CS and Co/NCS-T catalysts in Fig. 4b. The low temperature peak is ascribed to the reduction of CoO → Co for the Co/NCS-500 catalysts; while for the Co/CS and Co/NCS-T (T = 600, 700, 800) catalysts, the low temperature peak is ascribed to the overlapped reduction of Co<sub>3</sub>O<sub>4</sub> → CoO and subsequent CoO → Co. This low temperature peak does not show the apparent stepwise reductions of the conventional Co<sub>3</sub>O<sub>4</sub> pathway [45], which may be ascribed to the fact that the CoOx species of the catalysts mainly exist as CoO. The high temperature peak is ascribed to the gasification of the supports. Compared with the Co/CS catalyst, the reduction peak of cobalt oxides shifts to higher temperatures for all of the Co/NCS-T catalysts. The higher

temperature for reduction of cobalt species represents the stronger interaction between cobalt and support, which will induce the higher dispersion and smaller particle size of cobalt species. It indicates that doping heteroatom N can strengthen the interaction between cobalt and support. In addition, Co<sub>3</sub>O<sub>4</sub> shows a lower reduction temperature than CoO. Thus, the lowered reduction temperatures with the elevated carbonization temperatures for the Co/NCS-T catalysts should also partly result from the reduction of the varied cobalt species contents, as shown in Fig. 3.

Fig. 5 shows the TEM images of the reduced Co/NCS-T catalysts. Compared with the reduced Co/CS catalyst (Fig. 5e), the reduced Co/NCS-T catalysts exhibit the higher dispersion of the cobalt particles, because the doped N atoms can anchor metals [13,24]. The particle sizes of cobalt on the reduced Co/NCS-T catalysts increase with the decreased N contents. Especially, when the carbonization temperature exceeds 700 °C, the aggregated cobalt particles are clearly observed on the reduced Co/NCS-700 and Co/NCS-800 catalysts. The cobalt particles are enlarged, and the corresponding size distribution is broadened (inset in Fig. 5a–d) with the elevated carbonization temperatures, due to the weakened Co-N interaction strength. The stronger interaction is



**Fig. 5.** TEM images (inserted is the statistical histogram on particle sizes) of the reduced catalysts (a) Co/NCS-500, (b) Co/NCS-600, (c) Co/NCS-700, (d) Co/NCS-800, and (e) Co/CS; and (f) statistical histogram on particle sizes of the reduced Co/CS catalyst.

more favorable to anchor and disperse the cobalt particles. In addition, the dispersion of cobalt on the reduced Co/NCS-T catalysts estimated from the TEM results decreases from 14.8 to 10.1% with the elevated carbonization temperatures from 500 to 800 °C in Table 1.

### 3.3. Catalytic performance

The FTS catalytic performance of the as-prepared Co/CS and Co/NCS-T catalysts was evaluated in a fixed bed reactor, and Table 1 gives the related data. The effect of the support on the catalytic performance is clearly observed. In Table 1, as the carbonization temperature

increases from 500 to 800 °C, the cobalt-specific activity decreases from  $2.5 \times 10^{-5}$  to  $1.3 \times 10^{-5}$  mol<sub>CO</sub> g<sub>Co</sub><sup>-1</sup> s<sup>-1</sup>, the TOF value decreases from  $10.0 \times 10^{-3}$  to  $7.6 \times 10^{-3}$  s<sup>-1</sup>, the CH<sub>4</sub> selectivity slightly increases from 4.4 to 5.2%, and the C<sub>5</sub><sup>+</sup> selectivity decreases from 74.4 to 66.0%. Surprisingly, through adjusting the carbonization temperatures, we can tune the activity and selectivity of the Co/NCS-T catalysts in FTS. As compared with the Co/NCS-T catalysts under the same operating conditions, the Co/CS catalyst displays the lower activity including the cobalt-specific activity ( $1.0 \times 10^{-5}$  mol<sub>CO</sub> g<sub>Co</sub><sup>-1</sup> s<sup>-1</sup>) and the TOF ( $6.9 \times 10^{-3}$  s<sup>-1</sup>), the higher CH<sub>4</sub> selectivity (14.5%) and the lower C<sub>5</sub><sup>+</sup> selectivity (51.3%). It indicates that doping N atoms into the

**Table 1**  
Catalytic performance of the reduced catalysts in FTS.<sup>a</sup>

Catalysts	Co loading / %		$d(\text{Co}^*)$	$D$ / % <sup>b</sup>	Activity / $10^{-5} \text{ mol}_{\text{CO}} \text{ g}_{\text{Co}}^{-1} \text{ s}^{-1}$	TOF / $10^{-3} \text{ s}^{-1c}$	Selectivity / %			Olefin/Paraffin ratio <sup>d</sup>	$\alpha$
	TG	ICP					CH <sub>4</sub>	C <sub>2</sub> -C <sub>4</sub>	C <sub>5</sub> <sup>+</sup>		
Co/CS	2.9	3.0	11.1	8.6	1.0	6.9	14.5	34.2	51.3	0.51	0.57
Co/NCS-500	3.1	3.2	6.5	14.8	2.5	10.0	4.4	21.2	74.4	0.61	0.76
Co/NCS-600	3.3	3.2	7.8	12.3	1.9	9.1	4.3	26.2	69.5	0.60	0.72
Co/NCS-700	3.0	2.9	8.8	10.9	1.5	8.1	5.2	27.3	67.5	0.58	0.69
Co/NCS-800	2.9	2.9	9.5	10.1	1.3	7.6	5.2	28.8	66.0	0.57	0.68

<sup>a</sup> Reaction conditions: H<sub>2</sub>/CO = 2, 220 °C, 2.0 MPa, X<sub>CO</sub> < 10%.

<sup>b</sup> Metal dispersion.

<sup>c</sup> Determined from the cobalt-specific activity (A) and the dispersion of catalysts (D) using the following:  $\text{TOF} = 58.93 \times A \times D^{-1}$ .

<sup>d</sup> C<sub>2</sub>-C<sub>4</sub>.

carbon network remarkably enhances the activity of CO hydrogenation and the ability of carbon-chain growth.

### 3.4. Effect of N dopants on the FTS performance

Generally, contents and types of N dopants on supports will influence catalytic performances of catalysts [46–48]. As described previously, the N content accounted for all the elements in the sample decreases with the elevated carbonization temperatures. Fig. 6 shows the function of the N content on the FTS performance. The FTS activity and C<sub>5</sub><sup>+</sup> product selectivity increase with the increased N content in the catalysts. As well known, doping N atoms into carbon structures will provide chemically anchoring sites to increase metal dispersion [9,49]. Indeed, after comparing the TEM images of the reduced Co/NCS-T catalysts (Fig. 5a–d) and Co/CS (Fig. 5e), we observe that doping N into the carbon support is beneficial to improve the dispersion of metallic cobalt, which will increase the number of the active sites, leading to the enhanced activity [49,50]. In addition, the electron-rich N atoms on the support cause the transfer of electrons to the adjacent active cobalt sites, which facilitates dissociation of CO, to further enhance the catalytic activity [27,51].

The N 1s spectra of the NCS-T supports were deconvoluted to further illustrate the effect of N dopants on the FTS performance. Fig. 7 shows the high-resolution N 1s spectra of the samples. Three kinds of N dopants were deconvoluted, which are schematically shown in Fig. 7e: (i) pyridinic N (~398.4 eV) bonding with two carbon atoms in a six-membered ring with one *p*-electron localized in the  $\pi$  system, (ii) pyrrolic N (~400.3 eV) bonding with two carbon atoms in five-membered rings with two *p*-electrons, and (iii) graphitic N (~401.2 eV) substituting one C atom and bonding with three C atoms in the six-membered rings [52–54]. The peak deconvolution results show that the NCS-500 with the highest N content contains 22.9% pyridinic N, 73.9% pyrrolic N and 3.2% graphitic N; the NCS-600 contains 35.2% pyridinic

N, 58.7% pyrrolic N and 6.1% graphitic N; the NCS-700 contains 36.5% pyridinic N, 7.3% pyrrolic N and 56.2% graphitic N, and the NCS-800 contains 30.5% pyridinic N, 5.1% pyrrolic N and 64.4% graphitic N. Interestingly, the contents of the N dopants can be easily controlled by tuning the carbonization temperatures. Table S5. Thus, it can be concluded that the enhanced activity and C<sub>5</sub><sup>+</sup> selectivity are ascribed to the increased pyrrolic N content in the Co/NCS-T catalysts.

Figure S15 shows the XPS spectra of the Co/NCS-T catalysts. If the cobalt nanoparticles are selectively anchored on the N atoms, the surface N concentration will significantly decrease on the Co/NCS-T catalysts, compared with their corresponding supports, because of overlapping of cobalt on nitrogen. Figure S16 shows the total N content measured by XPS of the NCS-T supports and Co/NCS-T catalysts. The total N content of the Co/NCS-T catalysts is lower than that of the corresponding NCS-T supports in Figure S16. That is, loading cobalt on the NCS-T supports leads to a pronounced drop in the surface N concentration because of the priority nucleation of cobalt on the N sites. Fig. 8 shows the content of N dopants in the NCS-T supports and Co/NCS-T catalysts. For the NCS-500 support with the highest pyrrolic N content (6.3%) and the lowest graphitic N content (0.3%) which may be ignored, the pyrrolic N content decreases sharply after loading cobalt in Fig. 8a. For the NCS-600 support (Fig. 8b), the pyrrolic N content decreases by 28.5%, while the pyridinic N increases by 42.1% and the graphitic N increases slightly, compared with the NCS-500 support. At this point, we observe that the pyrrolic N and the pyridinic N decrease simultaneously after loading cobalt, demonstrating that when the amount of pyrrolic N atoms is reduced, pyridinic N also participates in anchoring cobalt. It indicates that pyrrolic N gives priority to anchor cobalt nanoparticles than pyridinic N. For the NCS-700 and NCS-800 supports (Fig. 8c–d), their pyrrolic N content is negligibly low, and we discover that the decrease in pyridinic N is greater than that of graphitic N after loading cobalt, indicating that the ability to anchor cobalt is pyridinic N > graphitic N. In summary, these discoveries suggest that the priority for anchoring cobalt nanoparticles follows the sequence of pyrrolic N > pyridinic N > graphitic N.

Fig. 9 shows the CO-TPD/MS profiles of the reduced Co/NCS-T catalysts. The desorption peak is ascribed to the desorption of recombination of the previously dissociated C\* and O\* species during CO adsorption on the cobalt sites [54,55]. In order to eliminate the influence of the carbon support, we performed the same CO-TPD/MS experiment on the NCS-500 support, and did not observe any CO desorption peak in Fig. 9. The amount of the desorbed CO increases as the pyrrolic N content increases in the Co/NCS-T catalysts, implying that the presence of pyrrolic N can generate more active cobalt sites to adsorb CO. Indeed, the TEM results in Fig. 5 show that the reduced Co/NCS-500 catalyst with the highest pyrrolic N content exhibits the highest dispersion (14.8%) of cobalt in the reduced Co/NCS-T catalysts, which will expose more active cobalt sites to adsorb more CO. In addition, it is noteworthy that although there is no significant difference in pyrrolic N content between the Co/NCS-700 and Co/NCS-

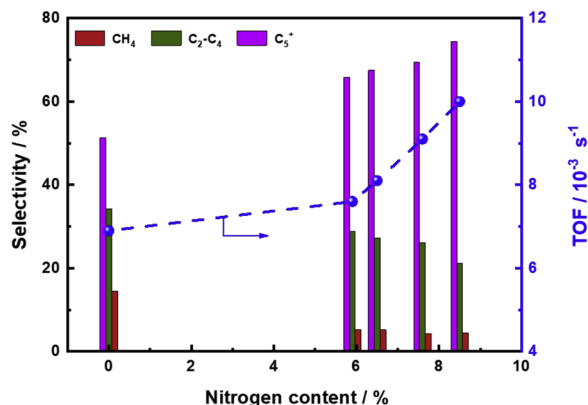


Fig. 6. Catalytic performances of the catalysts via the N contents.

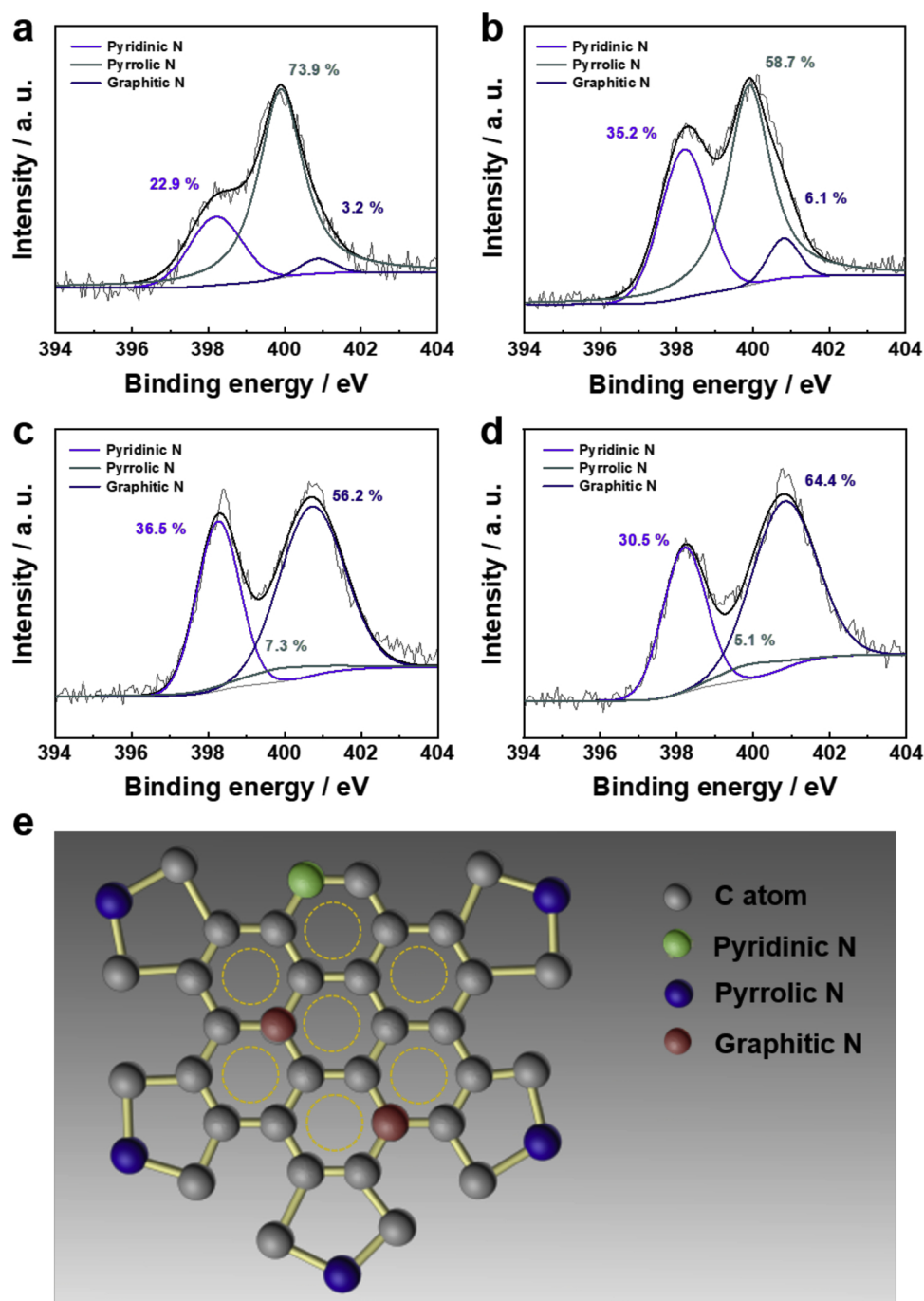


Fig. 7. N 1s XPS spectra of the supports (a) NCS-500, (b) NCS-600, (c) NCS-700, and (d) NCS-800; and (e) schematic illustration of the N dopants.

800 catalysts, the amount of desorbed CO on the former is larger than that on the latter. This may be caused by the high content of the pyridinic N and the low content of the graphitic N on the NCS-700 support in Table S5.

Moreover, the initial desorption temperatures of recombined CO increase from 318 to 339 °C as the pyrrolic N contents increase from 0.3 to 6.3% in the Co/NCS-T catalysts, indicating that the presence of pyrrolic N can strengthen the binding between C\* and active cobalt sites. The previous H<sub>2</sub>-TPR (Fig. 4) results show that the higher the pyrrolic N content, the stronger interaction between the cobalt and supports. That is, pyrrolic N strengthens the cobalt-support interaction, which facilitates the adsorption and dissociation of CO, resulting in elevation of the initial desorption temperatures of recombined CO [13]. Notably, the Co/NCS-700 catalyst with the high pyridinic N content and

the low graphitic N content exhibits the higher desorption temperatures than the Co/NCS-800 catalyst. It indicates that pyridinic N can induce a stronger binding strength between C\* and active cobalt sites than the graphitic N. The N dopants can significantly affect the local chemical environment of active cobalt sites via tailoring the interaction between the cobalt and supports resulting in the different Co-C bonding strength. Indeed, Bao's group [56] reported that both the pyrrolic and pyridinic N induced localized electronic states below the Fermi level in contrast to the graphitic N through DFT calculations, especially for pyrrolic N. Thus, the pyrrolic-N-induced electronic state possesses the highest energy level and density among all the N dopants, which facilitates CO adsorption on the Co/NCS-500 catalyst. The increased electron density of the active cobalt sites further promotes the dissociation and activation of CO via strengthening Co-C bond, promoting the FTS activity



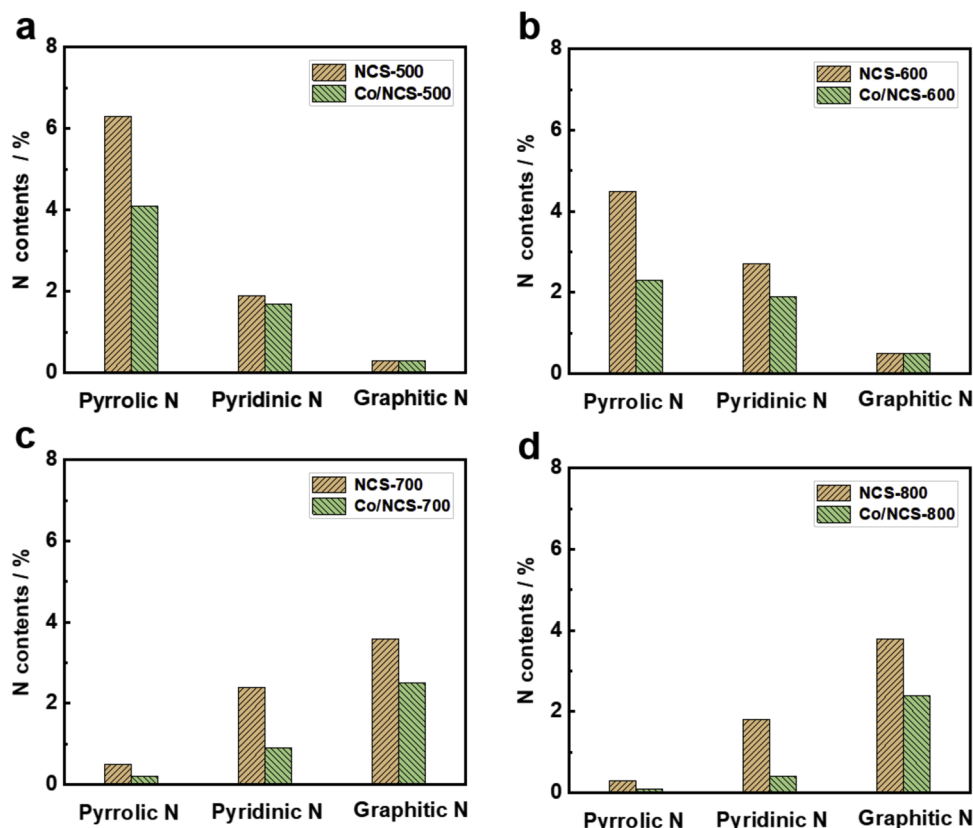


Fig. 8. N dopants molar content of the NCS-T supports and Co/NCS-T catalysts.

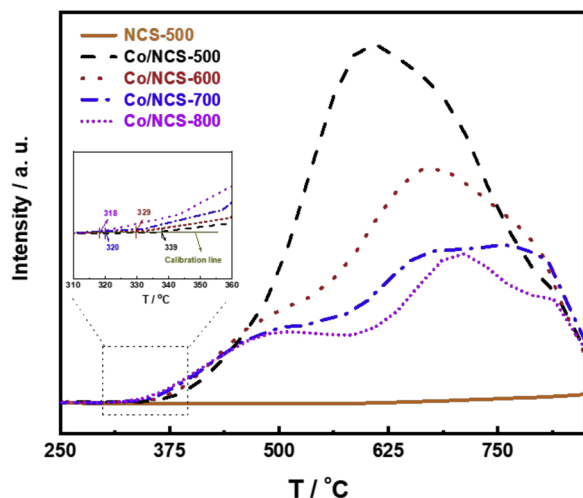


Fig. 9. CO-TPD/MS profiles of the reduced Co/NCS-T catalysts and the NCS-500 support.

[13,56]. Our results show that pyrrolic N plays the most important role in enhancing the activity of CO hydrogenation, followed by pyridinic N and then graphitic N.

The surface carbide mechanism is widely accepted to explain catalytic behaviors of FTS catalysts [57,58]. The chemisorbed  $C^*$  species from CO dissociation undergo hydrogenation to form chain initiator  $CH_2$  of carbon-chain growth and then follow C–C coupling by the surface carbide mechanism [57,59]. Notably, the  $CH_2$  coverage must be high enough to drive the carbon-chain growth. As discussed in Fig. 7, Table S5 and Figure S15, the Co/NCS-500 catalyst with the highest content of pyrrolic N can adsorb the highest concentration of activated  $C^*$ , which further facilitates the occurrence of the hydrogenation

reaction to form a high coverage of chain initiator  $CH_2$ , stimulating carbon-chain growth.

Figure S17 shows the extended X-ray absorption fine structure (EXAFS) results of the reduced Co/CS and Co/NCS-T catalysts. The EXAFS results in Figure S17 show the existence of the Co–N coordination shells, located at about 0.15 nm (uncorrected), over the reduced Co/NCS-T catalysts, indicating the presence of Co–N interaction [26,60]. Fig. 10 shows the *in situ* XPS Co 2p spectra of the pre-reduced Co/NCS-T and Co/CS catalysts. In Fig. 10, the BE peak located at about 778 eV is the characteristic of metallic cobalt. The BE peak positions of all the reduced Co/NCS-T catalysts are clearly lower than that of the reduced Co/CS catalyst (~778.0 eV) in Fig. 10, which further indicates that the N dopants can significantly change the chemical environment of the cobalt ascribed to electron-donor properties of N dopants,

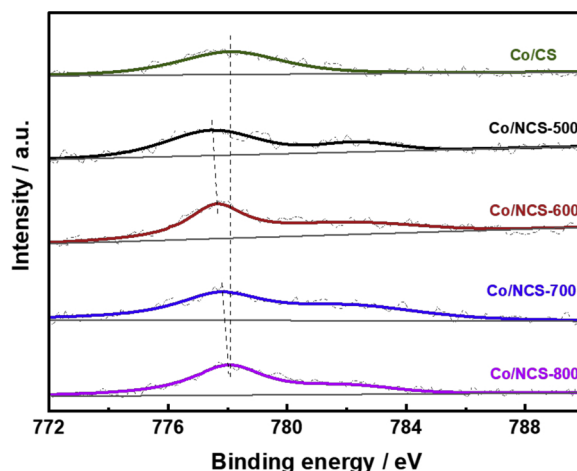


Fig. 10. *in situ* XPS spectra in the Co 2p<sub>3/2</sub> regions of the reduced catalysts.

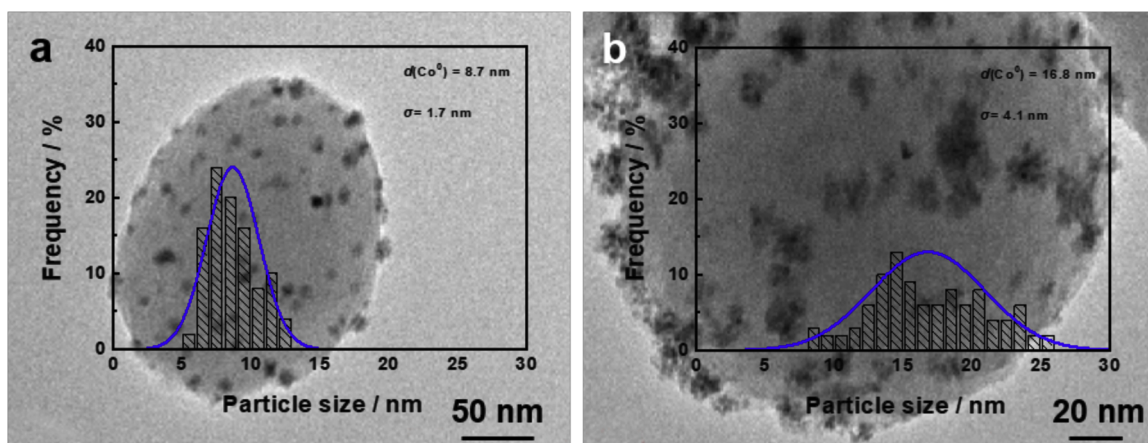


Fig. 11. TEM images (inserted is the statistical histogram on particle sizes) of the spent catalysts after the reaction for 50 h (a) Co/NCS-600 and (b) Co/NCS-700.

strengthening interaction between cobalt and support [61], as evidenced by the  $H_2$ -TPR (Fig. 4) results.

The BE peak positions of Co 2p gradually increase with the decreased pyrrolic N content in the reduced Co/NCS-T catalysts in Fig. 10. And compared with the reduced Co/CS catalyst, the largest offset up to  $\sim 0.45$  eV for the reduced Co/NCS-500 catalyst with the highest content of pyrrolic N among the reduced Co/NCS-T catalysts is ascribed to the occurrence of the electron transfer from the pyrrolic N to metallic cobalt [61], which induces the strongest interaction between cobalt and support among the catalysts.

On the basis of the above interpretations, we can demonstrate that the pyrrolic N in N dopants plays a leading role in tuning the interaction between cobalt and support. The controllable interaction will change the chemical environment of active cobalt sites and ultimately affect the catalytic performance. Pyrrolic N, which is enriched on the surface of NCS-500, is benefit to strengthen the interaction between the cobalt and support. The strengthened interaction improves the dispersion of metallic cobalt, which will expose more active cobalt sites to participate in activating CO and contribute to a higher catalytic activity. Moreover, during CO adsorption the electron-enriched cobalt sites resulting from the modification of pyrrolic N will strengthen the Co–C bond and weaken the C–O bond [13]. Thus, the dissociative adsorption of considerable CO and the subsequent formation of  $CH_2$  via hydrogenation ultimately stimulate C–C coupling reactions and produce heavy FTS products.

In addition, the strengthened Co–N interaction will effectively inhibit the aggregation of the cobalt catalysts in FTS. We compared the TEM images of the spent Co/NCS-600 (Fig. 11a) and Co/NCS-700 catalysts (Fig. 11b), because the NCS-600 (pyrrolic N: 4.5%) and NCS-700 (graphitic N: 3.6%) supports have the similar pyridinic N content ( $\sim 2.5\%$ ). The cobalt particles of the spent Co/NCS-600 catalyst were well dispersed (Fig. 11a), while those of the spent Co/NCS-700 catalyst (Fig. 11b) seriously aggregated. It indicates that the pyrrolic N dopants can effectively strengthen the interaction between cobalt and support via its donation electron function to inhibit the cobalt aggregation. In terms of stability, the Co/NCS-500 and Co/NCS-600 catalysts with the high pyrrolic N content remain stable after the reaction for 50 h, but the cobalt-specific activity of all other catalysts initially decreases and then maintains constant with the prolonged reaction time, as shown in Figure S18.

#### 4. Conclusions

In this work, a promising facile strategy is presented to controllable synthesis of N-doped carbon nanospheres supported cobalt catalysts. We can control the contents of the N dopants via adjusting the carbonization temperatures. The as-prepared N-doped carbon supports

display distinct advantages in anchoring and dispersing of cobalt species, which exhibit the enhanced activity and  $C_5^+$  product selectivity in FTS, following the sequence of pyrrolic N > pyridinic N > graphitic N. The pyrrolic N dopants generate the more pronounced Co-support interaction because of the occurrence of more electronic donation from pyrrolic N to cobalt. Our results show that the strengthened interaction on the Co/NCS-T catalysts significantly increases the number of electron-enriched cobalt sites. It not only promotes CO dissociation via weakening the C–O bond, but also increases the number of activated  $C^*$  species via improving the cobalt dispersion. Both of them guarantee a high concentration of chain initiators  $CH_2$  to boost up carbon-chain growth. This work clearly demonstrates the function of N dopants in FTS and provides an approach to rational design of related catalytic systems.

#### Declarations of interest

None.

#### Acknowledgments

The authors are grateful for financial support from the National Natural Science Foundation of China (No. 21676182, 21476159), the 973 program (2014CB932403), and the Program for Introducing Talents of Discipline to Universities of China (No. B06006).

#### Appendix A. Supplementary data

Supplementary material related to this article can be found, in the online version, at doi:<https://doi.org/10.1016/j.apcatb.2019.02.024>.

#### References

- [1] L. Zhong, F. Yu, Y. An, Y. Zhao, Y. Sun, Z. Li, T. Lin, Y. Lin, X. Qi, Y. Dai, L. Gu, J. Hu, S. Jin, Q. Shen, H. Wang, *Nature* 538 (2016) 84–87.
- [2] Q. Zhang, J. Kang, Y. Wang, *ChemCatChem* 2 (2010) 1030–1058.
- [3] X. Sun, A.I.O. Suarez, M. Meijerink, T. van Deelen, S. Ould-Chikh, J. Zečević, K.P. de Jong, F. Kapteijn, J. Gascon, *Nat. Commun.* 8 (2017) 1680–1687.
- [4] V.P. Santos, T.A. Wezendonk, J.J.D. Jaén, A.I. Dugulan, M.A. Nasalevich, H.-U. Islam, A. Chojeci, S. Sartipi, X. Sun, A.A. Hakeem, A.C.J. Koeken, M. Ruitenbeek, T. Davidian, G.R. Meima, G. Sankar, F. Kapteijn, M. Makkee, J. Gascon, *Nat. Commun.* 6 (2015) 6451–6458.
- [5] Q. Cheng, Y. Tian, S. Lyu, N. Zhao, K. Ma, T. Ding, Z. Jiang, L. Wang, J. Zhang, L. Zheng, F. Gao, L. Dong, N. Tsubaki, X. Li, *Nat. Commun.* 9 (2018) 3250–3258.
- [6] L. Zhang, Z. Xia, *J. Phys. Chem. C* 115 (2011) 11170–11176.
- [7] D.S. Su, S. Perathoner, G. Centi, *Chem. Rev.* 113 (2013) 5782–5816.
- [8] Y. Xu, C. Zhang, M. Zhou, Q. Fu, C. Zhao, M. Wu, Y. Lei, *Nat. Commun.* 9 (2018) 1720–1820.
- [9] N. Daems, J. Wouters, C. Van Goethem, K. Baert, C. Poleunis, A. Delcorte, A. Hubin, I.F.J. Vankelecom, P.P. Pescarmona, *Appl. Catal. B Environ.* 226 (2018) 509–522.
- [10] D. Guo, R. Shibuya, C. Akiba, S. Saji, T. Kondo, J. Nakamura, *Science* 351 (2016)

- 361–365.
- [11] P. Zhang, Y. Gong, H. Li, Z. Chen, Y. Wang, *Nat. Commun.* 4 (2013) 1593–1603.
  - [12] C. Genovese, M.E. Schuster, E.K. Gibson, D. Gianolio, V. Posligua, R. Grau-Crespo, G. Cibir, P.P. Wells, D. Garai, V. Solokha, S. Krick Calderon, J.J. Velasco-Velez, C. Ampelli, S. Perathoner, G. Held, G. Centi, R. Arrigo, *Nat. Commun.* 9 (2018) 935–946.
  - [13] J. Lu, L. Yang, B. Xu, Q. Wu, D. Zhang, S. Yuan, Y. Zhai, X. Wang, Y. Fan, Z. Hu, *ACS Catal.* 4 (2014) 613–621.
  - [14] M. Davari, S. Karimi, A. Tavasoli, A. Karimi, *Appl. Catal. A Gen.* 485 (2014) 133–142.
  - [15] H. Xiong, M.A. Motchelaho, M. Moyo, L.L. Jewell, N.J. Coville, *Appl. Catal. A Gen.* 482 (2014) 377–386.
  - [16] T. Fu, Z. Li, *Catal. Commun.* 47 (2014) 54–57.
  - [17] T. Fu, R. Liu, Z. Li, *Fuel Process. Technol.* 122 (2014) 49–57.
  - [18] Z. Li, R. Liu, Y. Xu, X. Ma, *Appl. Surf. Sci.* 347 (2015) 643–650.
  - [19] T. Fu, Z. Li, *Chem. Eng. Sci.* 135 (2015) 3–20.
  - [20] H. Xiong, M. Moyo, M.A. Motchelaho, Z.N. Tetana, S.M.A. Dube, L.L. Jewell, N.J. Coville, *J. Catal.* 311 (2014) 80–87.
  - [21] H. Xiong, M. Moyo, M. Rayner, L. Jewell, D. Billing, N. Coville, *ChemCatChem* 2 (2010) 514–518.
  - [22] X. Chen, D. Deng, X. Pan, X. He, *Chem. Commun.* 51 (2015) 217–220.
  - [23] S. Taghavi, A. Asghari, A. Tavasoli, *Chem. Eng. Res. Des.* 119 (2017) 198–208.
  - [24] Y. Yang, L. Jia, B. Hou, D. Li, J. Wang, Y. Sun, *ChemCatChem* 6 (2013) 319–327.
  - [25] M. Oschatz, J. Hofmann, T. van Deelen, W. Lamme, N. Krans, E. Hensen, K. de Jong, *ChemCatChem* 9 (2017) 620–628.
  - [26] B. Qiu, C. Yang, W. Guo, Y. Xu, Z. Liang, D. Ma, R. Zou, *J. Mater. Chem. A* 5 (2017) 8081–8086.
  - [27] Y. Yang, L. Jia, B. Hou, D. Li, J. Wang, Y. Sun, *J. Phys. Chem. C* 118 (2014) 268–277.
  - [28] P. Chen, F. Yang, A. Kostka, W. Xia, *ACS Catal.* 4 (2014) 1478–1486.
  - [29] W. Xia, *Catal. Sci. Technol.* 6 (2016) 630–644.
  - [30] X. Ning, Y. Li, B. Dong, H. Wang, H. Yu, F. Peng, Y. Yang, *J. Catal.* 348 (2017) 100–109.
  - [31] Y. Sun, I. Sinev, W. Ju, A. Bergmann, S. Dresch, S. Köhl, C. Spöri, H. Schmies, H. Wang, D. Bernsmeier, B. Paul, R. Schmack, R. Kraehnert, B. Roldan Cuenya, P. Strasser, *ACS Catal.* 8 (2018) 2844–2856.
  - [32] K. Ai, Y. Liu, C. Ruan, L. Lu, G. Lu, *Adv. Mater.* 25 (2012) 998–1003.
  - [33] X. Su, Y. Li, *Angew. Chem. Int. Ed.* 43 (2004) 597–601.
  - [34] B. Zeng, B. Hou, L. Jia, J. Wang, C. Chen, D. Li, Y. Sun, *Catal. Sci. Technol.* 3 (2013) 3250–3255.
  - [35] R.C. Reuel, C.H. Bartholomew, *J. Catal.* 85 (1984) 63–77.
  - [36] H. Lee, S.M. Dellatore, W.M. Miller, P.B. Messersmith, *Science* 318 (2007) 426–430.
  - [37] L. Zhang, J. Wu, Y. Wang, Y. Long, N. Zhao, J. Xu, *J. Am. Chem. Soc.* 134 (2012) 9879–9881.
  - [38] I. Moon, J. Lee, R. Ruoff, H. Lee, *Nat. Commun.* 73 (2010) 1067–1072.
  - [39] L. Li, P. Dai, X. Gu, L. Yan, X. Zhao, *J. Mater. Chem. A* 5 (2017) 789–795.
  - [40] J. Zhao, P.A. Montano, *Phys. Rev. B* 40 (1989) 3401–3404.
  - [41] S. Sun, N. Tsubaki, K. Fujimoto, *Appl. Catal. A Gen.* 202 (2000) 121–131.
  - [42] G.-Z. Bian, N. Fujishita, T. Mochizuki, W.-S. Ning, M. Yamada, *Appl. Catal. A Gen.* 252 (2003) 251–260.
  - [43] H. Xiong, M.A.M. Motchelaho, M. Moyo, L.L. Jewell, N.J. Coville, *J. Catal.* 278 (2011) 26–40.
  - [44] K. Xiong, J. Li, K. Liew, X. Zhan, *Appl. Catal. A Gen.* 389 (2010) 173–178.
  - [45] K. Cheng, V. Subramanian, A. Carvalho, V.V. Ordonsky, Y. Wang, A.Y. Khodakov, *J. Catal.* 337 (2016) 260–271.
  - [46] T. Lin, I.W. Chen, F. Liu, C. Yang, H. Bi, F. Xu, F. Huang, *Science* 350 (2015) 1508–1513.
  - [47] Y. Ito, W. Cong, T. Fujita, Z. Tang, M. Chen, *Angew. Chem. Int. Ed.* 127 (2014) 2159–2164.
  - [48] R. Jaiswal, J. Bharambe, N. Patel, A. Dashora, D.C. Kothari, A. Miotello, *Appl. Catal. B Environ.* 168–169 (2015) 333–341.
  - [49] K. Chizari, I. Janowska, M. Houllé, I. Florea, O. Ersen, T. Romero, P. Bernhardt, M.J. Ledoux, C. Pham-Huu, *Appl. Catal. A Gen.* 380 (2010) 72–80.
  - [50] J.H. den Otter, H. Yoshida, C. Ledesma, D. Chen, K.P. de Jong, *J. Catal.* 340 (2016) 270–275.
  - [51] S. Li, N. Yao, F. Zhao, X. Li, *Catal. Sci. Technol.* 6 (2016) 2188–2194.
  - [52] L. Qie, W. Chen, H. Xu, X. Xiong, Y. Jiang, F. Zou, X. Hu, Y. Xin, Z. Zhang, Y. Huang, *Energy Environ. Sci.* 6 (2013) 2497–2504.
  - [53] Z. Li, J. Liu, C. Xia, F. Li, *ACS Catal.* 3 (2013) 2440–2448.
  - [54] J. Zhang, L. Ma, S. Fan, T. Zhao, Y. Sun, *Fuel* 109 (2013) 116–123.
  - [55] X. Yu, J. Zhang, X. Wang, Q. Ma, X. Gao, H. Xia, X. Lai, S. Fan, T.-S. Zhao, *Appl. Catal. B Environ.* 232 (2018) 420–428.
  - [56] X. Li, X. Pan, L. Yu, P. Ren, X. Wu, L. Sun, F. Jiao, X. Bao, *Nat. Commun.* 5 (2014) 3688–3694.
  - [57] M. Ojeda, R. Nabar, A.U. Nilekar, A. Ishikawa, M. Mavrikakis, E. Iglesia, *J. Catal.* 272 (2010) 287–297.
  - [58] H.M. Torres Galvis, K.P. de Jong, *ACS Catal.* 3 (2013) 2130–2149.
  - [59] J. Yang, W. Ma, D. Chen, A. Holmen, B.H. Davis, *Appl. Catal. A Gen.* 470 (2014) 250–260.
  - [60] X. Sun, A.I. Olivos-Suarez, D. Osadchii, M.J.V. Romero, F. Kapteijn, J. Gascon, *J. Catal.* 357 (2018) 20–28.
  - [61] L. Guo, W. Jiang, Y. Zhang, J. Hu, Z. Wei, L. Wan, *ACS Catal.* 5 (2015) 2903–2909.